IEEE Photonics Journal
An IEEE Photonics Society Publication

Open Access

Programmable Multiwavelength Achromatic Focusing and Imaging Through Scattering Media

Volume 10, Number 5, September 2018

Jietao Liu
Jiannan Wang
Wei Li
Xueying Sun
Lei Zhu
Chengfei Guo
Xiaopeng Shao

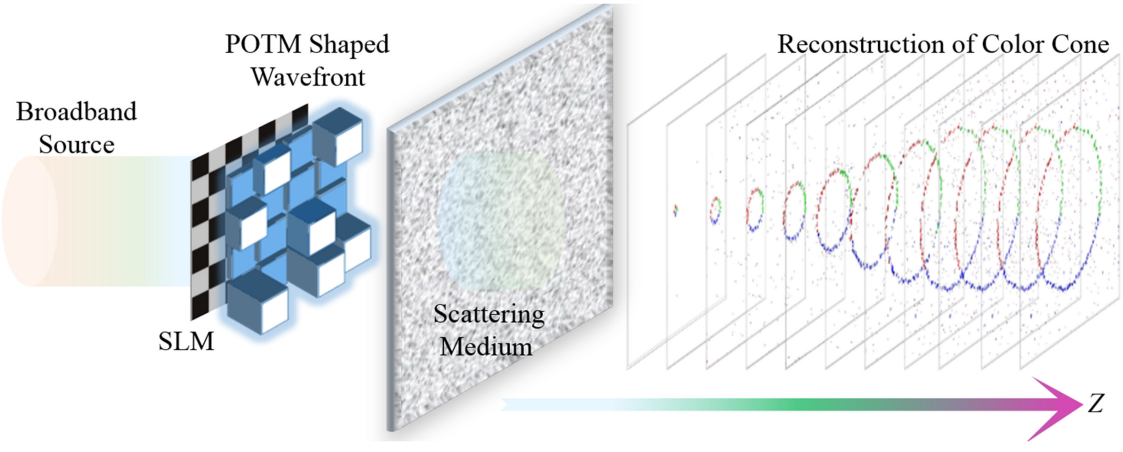

DOI: 10.1109/JPHOT.2018.2865518
1943-0655

IEEE photonics SOCIETY

IEEE

Programmable Multiwavelength Achromatic Focusing and Imaging Through Scattering Media

Jietao Liu, Jiannan Wang, Wei Li, Xueying Sun, Lei Zhu, Chengfei Guo, and Xiaopeng Shao

School of Physics and Optoelectronic Engineering, Xidian University, Xi'an 710071, China

DOI:10.1109/JPHOT.2018.2865518

Manuscript received June 10, 2018; revised July 31, 2018; accepted August 10, 2018. Date of publication August 23, 2018; date of current version September 21, 2018. This work was supported in part by the National Natural Science Foundation of China under Grants 61575154 and 11704299 and in part by the Fundamental Research Funds for the Central Universities (SA-ZD160501) and the 111 project (B17035). Corresponding author: Jietao Liu (email: jtliu09@semi.ac.cn).

Abstract: Optical imaging and focusing through complex samples is a challenge with important applications in many fields. The critical problem is that turbid media such as biological tissue and multimode optical fibers randomly scatter and diffuse light, preventing the formation of diffraction-limited focus and image. We demonstrate with numerical simulations that a multiple scattering can be controlled via a serial optical transmission matrix and a parallel optical transmission matrix in order to obtain an achromatic focus and image at an arbitrary position. Simulation results of three-dimensional achromatic focusing and imaging based on this approach are agreed with the theoretical analysis. A scattering diffuser can be used as functional optical elements for focusing and imaging, moreover it can be manipulated and designed for multifunctional optical elements beyond traditional design. Our method will pave a way for using scattering media as unique optical achromatic elements for various applications, as well as for guiding the light and tailoring the light field.

Index Terms: Wavefront control, optical achromatic element, multiple scattering, scattering media, transmission matrix.

1. Introduction

For long the scattering of light is treated as an obstacle for optical focusing and imaging, where the light scattering posed a fundamental limitation on the resolution and penetration depth of all optical methods [1]. Nowadays, Scattering media have been studied for applications of the focusing [2]–[8], spectral filter [9], [10], photorefractive holography [11] and biomedical imaging [12]–[18]. To date, a significant number of techniques such as wavefront shaping [1], [5], [17], [19], [20], speckle correlation imaging [21]–[24], deblur processing [25], [26], deep learning [27], [28],scattering holography [29]–[32] and transmission matrix approach [20], [21] have been developed to explore the characters of scattering media or optical shaping and manipulation, which give variety of new realm in traditional optical imaging technology.

However, benefit from lensless and non-invasive advantages, speckle correlation methods restores crucial autocorrelation information after scattering, which unfortunately is limited by tiny angular memory effect range and narrow illumination spectral width [21]–[24]. What's more, inspired by applied optics, deblur technique [25], [26], based on imaging post-processing, can only

work in correcting low-order aberrations under weak scattering region of a superposition of specific noisy models. Simultaneously, with holography one can image 3D structure through dynamic media [29]–[32], however, it meanwhile requires prior reference, strict positional alignment of the hologram and the read-out beam. Ingeniously, deep learning strategy is used to study for scattering imaging [27], [28]. Although we can get high fidelity of image transferred through scattering media, deep learning methods relies heavily on mountain piled training database and arcane network parameter tuning process. Shaping the wavefront by means of seeking the optimal wavefront by various feedback algorithms [20] or compensating for the scattering media, light can be focused through or deep inside the strongly scattering materials directly observed anywhere on the detector, and the scattering media can be used as functional optical elements. However, the scanning and updating process for only a focusing point is very time-consuming, making it not suitable for in-vivo imaging. Moreover, the optical TM inherently characterizes the scattering medium by giving the relationship between the input and the output wave [20], [21], with which one can use it to directly recover the object wave for imaging from the distorted speckles though it is prone to errors for a little deviation or perturbation of the measurement may seriously influence the final imaging quality.

Overall, most methods mentioned above, to some degree, neglect the study of spectra, which offers a plethora of contrast mechanisms in imaging and spectroscopy, especially for those who study scattering media and their interaction with the waves. Since programmable controlled achromatic three-dimension (3D) image and focus through scattering media are much desired both in spatial and spectrum domain, here with the aid of advantages of wavefront shaping and transmission matrix, we intended to focus and image an object hidden behind a turbid medium. This is promising for full control and customized guiding of light for next stage light-matter interaction and applications.

In this paper, we put forward an arbitrary phase shifts (APS) to measure the monochromatic optical transmission matrix (MOTM) of scattering media with an easy-to-build setup, and efficient computational process. It also has a pivotal role in eliminating the requirements of the modulation depth of spatial light modulator together with the advantage of unrestricted implementation regardless of memory effect. Furthermore, we introduce the simulation system and establish serial optical transmission matrix (SOTM) and parallel optical transmission (POTM) for achromatic focusing through scattering media by wavefront shaping in different distances between scattering media and detector, i.e., achromatic 3D focusing and imaging through scattering media, as well as showing achromatic 3D focusing and imaging results of the targets beyond memory effect. The results shed new light on extending the source to broadband and achieving multiwavelength achromatic focusing and imaging using scattering elements.

2. Principle of Obtaining SOTM, POTM and Achromatic Focusing

2.1 Acquisition of MOTM by APS Method

Inspired by full-field interferometric method to measure the TM proposed by Popoff [33], we actually measured MOTM with APS based on it. When an optimal wavefront is found and impinged upon, a desired optical field can be obtained after the turbid media, and light focusing and imaging through turbid medium at any position of the output can be obtained [34], [35].

Even though light scatters in a complex and initially unknown way, the scattering process is linear and entirely deterministic as long as the medium is static [33]. A linear propagation of an optical wave through scattering media is entirely characterized by Green function, and the wavelength-dependent transmission of light through scattering media can be expressed as:

$$(E_m^{\text{out}})_{\lambda_i} = \sum_{n}^{N} (t_{mn})_{\lambda_i} E_n^{\text{in}}, (i = 1, 2 \ldots..). \tag{1}$$

where the complex coefficients $(t_{mn})_{\lambda_i}$ of MOTM link the input optical field $\mathbf{E}_n^{\text{in}}$ at the nth input element and output optical field $\mathbf{E}_m^{\text{out}}$ at the mth output element at λ_i.

Thanks to the interferometry [36], we can achieve phase of optical field indirectly. Here, the real part of MOTM is represented as a, correspondingly imaginary part as b, and thereafter the intensity

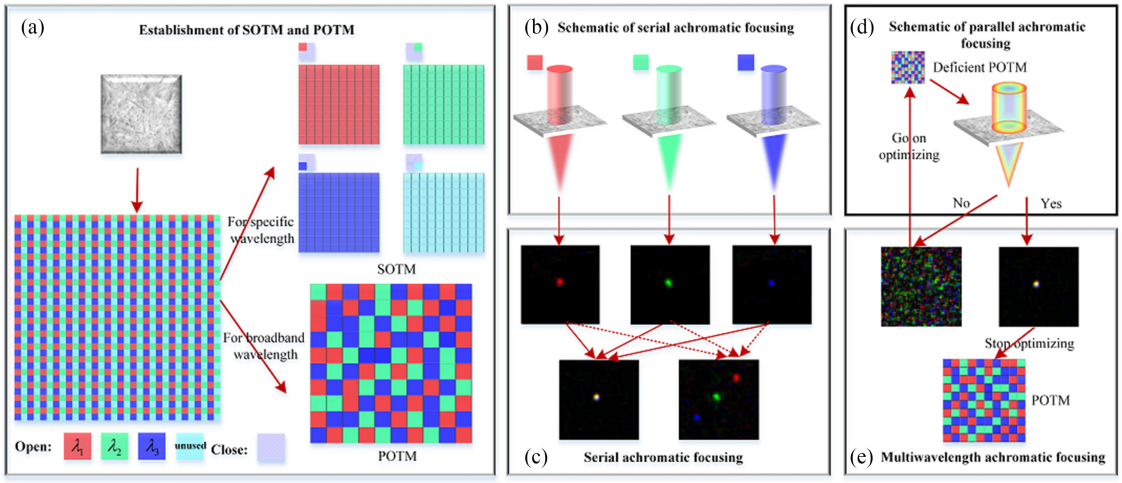

Fig. 1 Schematic of establishing SOTM, POTM and focusing: (a), (b) and (d) are schematic diagrams of SOTM or POTM, serial achromatic focusing, and parallel achromatic focusing respectively. (c) and (e) are results of serial achromatic focusing and multi-wavelength achromatic focusing, respectively.

detected by the detector can be expressed as:

$$
\begin{aligned}
(\mathbf{I}_m^p)_{\lambda_i} &= \left|(\mathbf{E}_m^{\text{out}})_{\lambda_i}\right|^2 = \left|r_m + \sum_n e^{jp}(t_{mn})_{\lambda_i}\mathbf{E}_n^{\text{in}}\right|^2 \\
&= \left|e^{j\theta}\right|^2 + \left|\sum_n e^{jp}(t_{mn})_{\lambda_i}\mathbf{E}_n^{\text{in}}\right|^2 + 2\text{Re}(e^{jp}e^{j\theta}\sum_n (t_{mn})_{\lambda_i}\mathbf{E}_n^{\text{in}}) \\
&= \left|e^{j\theta}\right|^2 + \left|\sum_n e^{jp}(t_{mn})_{\lambda_i}\mathbf{E}_n^{\text{in}}\right|^2 + 2\cos(p+\theta)\times a - 2sin(p+\theta)\times b, \qquad (2)
\end{aligned}
$$

where r_m is the complex amplitude of the optical field with a phase of θ and used as the reference in the mth output mode, and p is the arbitrary shift of phase to form an interference.

Owing to that E_n^{in} is controllable, we can solve the complex coefficients t_{mn} in $2N$ times, where N is the input channels. For maximizing the intensity of the received wave front and consequently decreasing the experimental sensibility to noise, a Hadamard basis is introduced to help us modulate only the phase of optical field. Additionally, benefit from the arbitrary phase of α and β, the modulation depth of the SLM is unrestricted. For obtaining a canonical matrix (expressed as T^d) to focusing and imaging, a basis exchange, $T^d = T^h \times T^{\dagger}$, is used, where h denotes Hadamard basis, T^h and T^d is the MOTM in Hadamard and Cartesian basis, respectively. † describes transpose conjugate.

2.2 Acquisition of SOTM and POTM for Achromatic Focusing

The schematic of establishing SOTM and POTM from MOTMs together with principle of achromatic focusing are illustrated in Fig. 1. For establishing a SOTM or POTM with MOTMs, we divide the scattering medium into $N \times N$ equally squared cells, where each cell is subdivided into 2×2 small segments (see Fig. 1(a)) for different channels. In the case of forming a SOTM, we artificially select out the channels of red, green and blue for color focusing (see Fig. 1(b)), respectively. When three appointed focusing positions are overlapped, the foci is achromatic, otherwise the focus are individually as depicted in Fig. 1(c).

Alternatively, we create a POTM by randomly closing or opening the segments of cells equally to complete an achromatic focusing parallel by wave shaping at arbitrary position with only one

transmission matrix as shown in Fig. 1(d). Moreover, the parallel achromatic focusing (see Fig. 1(e)) can be achieved by the loop shown in Fig. 1(d). Once the foci is perfectly achromatic accomplished, we obtain the POTM. By adjusting the target function used for feedback, optimized multiple foci can be accomplished simultaneously. For the sake of getting maximum enhancement factor and minimum focusing error concurrently, the targets function is defined as:

$$F(\lambda, d, P, P') = \max \sum_{i=1}^{3} \frac{\eta_{\lambda_i}}{(P_{\lambda_i}(x, y) - P'_{\lambda_i}(x, y))}\Bigg|_{d=d_z}.$$

s.t.

$$c(\lambda_i) \geq 1/3 \times col \times row.$$

$$\frac{\pi}{4}(N-1)+1 > \eta_{\lambda_i} > \frac{1}{2} \times \left(\frac{\pi}{4}(N-1)+1\right). \; i = 1, 2, 3 \tag{3}$$

where F is objective function of λ, the focusing position, and the distance d between SLM and detector. c describes certain wavelength's segments, *col* and *row* express the column and row of subdividing square cells, respectively. $P_{\lambda_i}(x, y)$, $P'_{\lambda_i}(x, y)$ are the designed focusing target's position and the obtained actual position for λ_i, respectively; η_{λ_i} is enhancement factor for λ_i and $dz = 22$ cm.

3. Experimental Setup and Simulation Process

Three laser sources with different wavelengths (478 nm, 532 nm and 628 nm) are first intensity attenuated to ensure comparable power levels and then guided into a single path using beam splitters. After expanded and polarization modulated, the beams simultaneously illuminate a spatial light modulator (SLM) (VIS-016, Holoeye Pluto, Germany) during the entire experiment. For projecting the phase of SLM onto the scattering sample, which is a 80 μm layer of ZnO deposited on a standard microscope glass slide, the SLM is positioned at a conjugate image plane of the first microobjective (10×, NA = 0.25). The pixel number of SLM is 1920 × 1080, only the central 512 × 512 portion is used in the experiments. A second microobjective (40×, NA = 0.65) imaged the plane 1 mm behind the scattering media, as well as collecting the scattering light. The two microscope objectives are used for the purpose of efficiently collecting optical channels of light through scattering medium. The speckle is captured by a CMOS detector (Andor Zyla 5.5), before which is a polarizing film used to remove the ballistic light.

The optical transmission simulation process in Fig. 2(a) can be characterized as schematic in Fig. 2(b). The scattering sample is inserted at a distance d_1 in front of the detector. Distance between SLM and scattering sample is d_1 and d from scattering sample to the detector. Here, we mathematically approximate the scattering media as a thin phase mask whose amplitude transmittance is 1 and phase is $\phi(x, y)$. Besides, coefficients in MOTM must be statistically independent and follow a circular Gaussian distribution [3], [37] according to the corresponding principle of statistical optics [38]. In this case, a forward model can be derived to relate the optical field at the detector plane $U(x, y)$ to the optical field at the object plane $U_{SLM}(x_o, y_o)$, (constant terms have been neglected). Furthermore, by exploiting light free space transmission based on Angular-Spectrum Propagation theory, the modulated field propagation from the SLM to the front of scattering sample can be described by,

$$U_s(x_s, y_s) = \mathcal{F}^{-1}\left\{\mathcal{F}\{U_{SLM}(x_o, y_o)\} \exp\left[-ikd_1\sqrt{1-(\lambda f_{x_s})^2-(\lambda f_{y_s})^2}\right]\right\}, \tag{4}$$

where k is the modulus of the wave vector $k = 2\pi/\lambda$, λ represents light wavelength.f_{x_s} and f_{y_s} are coordinates in frequency domain. As expected, the propagation from the background of scattering sample to CCD can be described by,

$$U(x, y) = \mathcal{F}^{-1}\left\{\mathcal{F}\{U'_s(x_s, y_s)\} \exp\left[-ikd\sqrt{1-(\lambda f_x)^2-(\lambda f_y)^2}\right]\right\}, \tag{5}$$

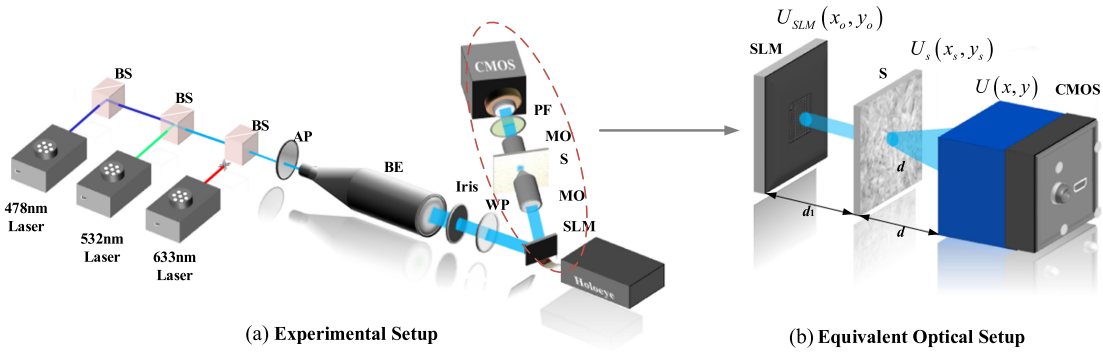

(a) **Experimental Setup** (b) **Equivalent Optical Setup**

Fig. 2 Experimental Setup and equivalent simulation part: (a) Experimental Setup. Lasers power and polarization from a 478 nm, a 532 nm and a 633 nm laser are attenuated, expanded and reflected off an SLM. Wave plate selects a phase-only modulation mode. The modulated beam is focused on the multiple-scattering sample and the output intensity speckle pattern is imaged by a CCD camera. L, lens; D, diaphragm; S, sample; MO, microscope objective; PF, polarizing film; BS, beam splitter; AP, Attenuation piece; BE, beam expander; WP, waveplate.(b) Simulation for circle part of (a). Light from a multispectral object shown on a SLM ($\sum_o$) propagating through scattering media (distance d1) and generates a speckle pattern on detector ($\sum_i$).

TABLE 1
Simulation Setup for Fig. 2 (b)

Parameters	Values
Wavelength	0.478μm、0.532μm、0.628μm
Size of SLM pixels array	5mm×5mm
Pixels of SLM	N×N
Spatial sampling interval	12.2μm
Modulated size of SLM	3.125mm×3.125mm
Modulated pixels of SLM	(0.625×N)×(0.625×N)
Size of scattering medium	1mm×1mm
d_1	1000mm
d	220mm
Number of cells of the modulated part of SLM	$\sqrt{N}\times\sqrt{N}$
size of detector	1.1mm×1.1mm
Used size of detector	(FWHM × $\sqrt{N}$)×(FWHM × $\sqrt{N}$)
Pixel size of detector	4.2μm
Number of segments of used part of detector	$\sqrt{N}\times\sqrt{N}$

where $U'_s(x_s, y_s) = U_s(x_s, y_s) \times e^{j\phi(x_s,y_s)}$. It is noted that $U(x, y)$ and $U_{SLM}(x_o, y_o)$ are the same as $\mathbf{E}^{\text{out}}$ and $\mathbf{E}^{\text{in}}$ in Eq. (1), respectively.

According to the restrictions and modals above, we establish the scattering optical system. The primary simulation parameters are listed in Table 1, based on which and the MOTMs in Section 2.1 we can establish SOTM, POTM and obtain an achromatic 3D focusing as well as achromatic imaging.

4. Numerical Simulation Results and Analysis

According to the principle in Section 2, we achieve SOTM and POTM, after which we have done some single point focusing with different incident wavelengths in Fig. 3(a).

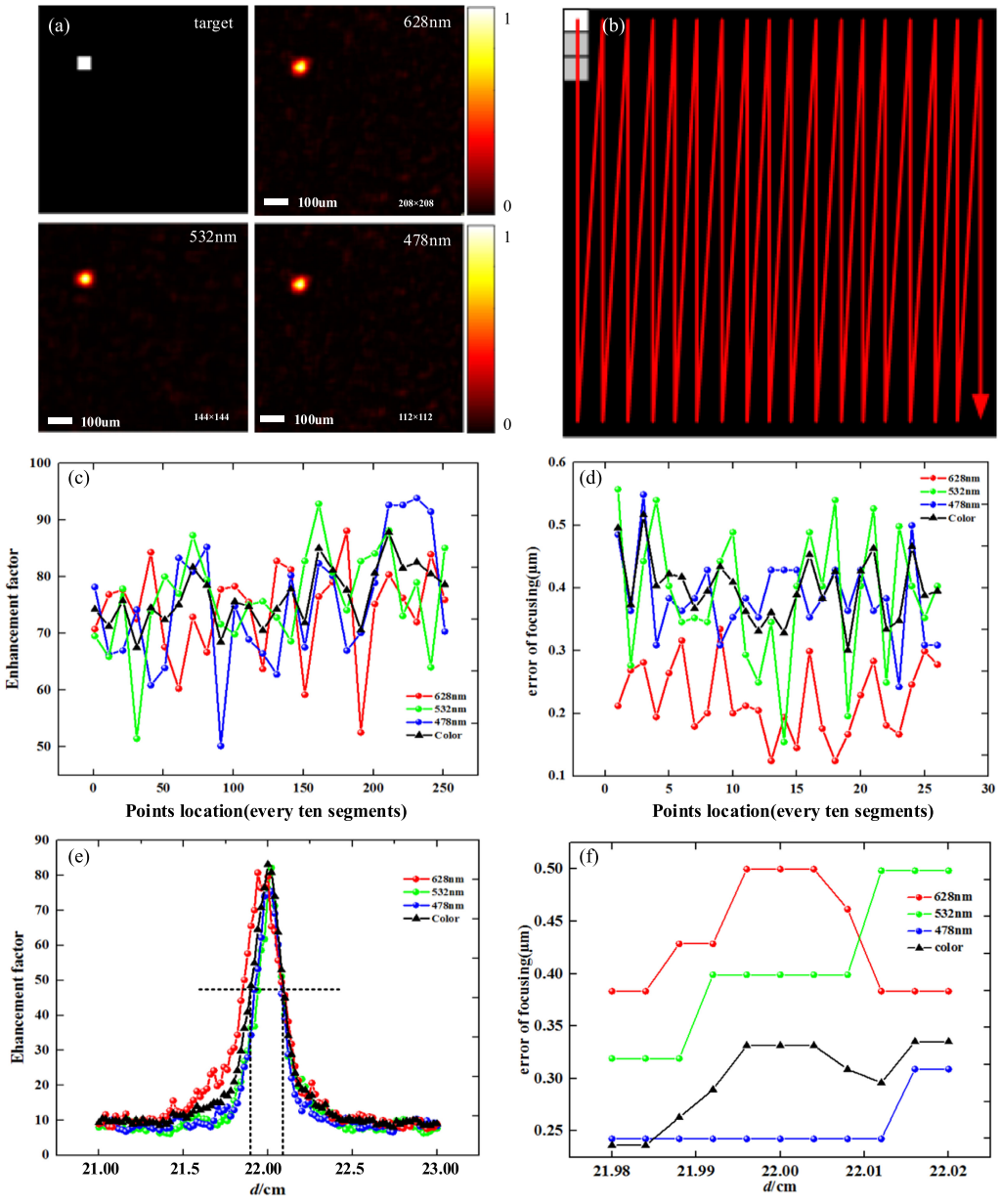

Fig. 3 Results and analysis of monochromatic focusing: (a) Single point monochromatic focusing of target when $\lambda = 628$ nm, 532 nm, and 478 nm. (b) A linear fashion rastering over the two-dimensional pixel arrays for focusing in every segments of the detector. (c), (e) are enhancement factors for different wavelength in different points position (every ten segments) on detector and depth of focus for monochromatic focusing, respectively. (d), (f) are error sizes for (c) and (e), respectively. Scale-bar of (a) is 100 μm.

If the segment size of detector is less than the coherence length, two neighboring segments will be strongly correlated [34]. Coherence length of speckle is calculated as the full width at half-maximum (FWHM) of the auto-correlation of the speckle pattern at each working waves. Without loss of generality, incident light can be expressed as:

$$f(x, \lambda) = \frac{1}{\sigma_\lambda \sqrt{2\pi}} \exp\left[-\frac{(x - x_0)^2}{2\sigma_\lambda^2}\right], \tag{6}$$

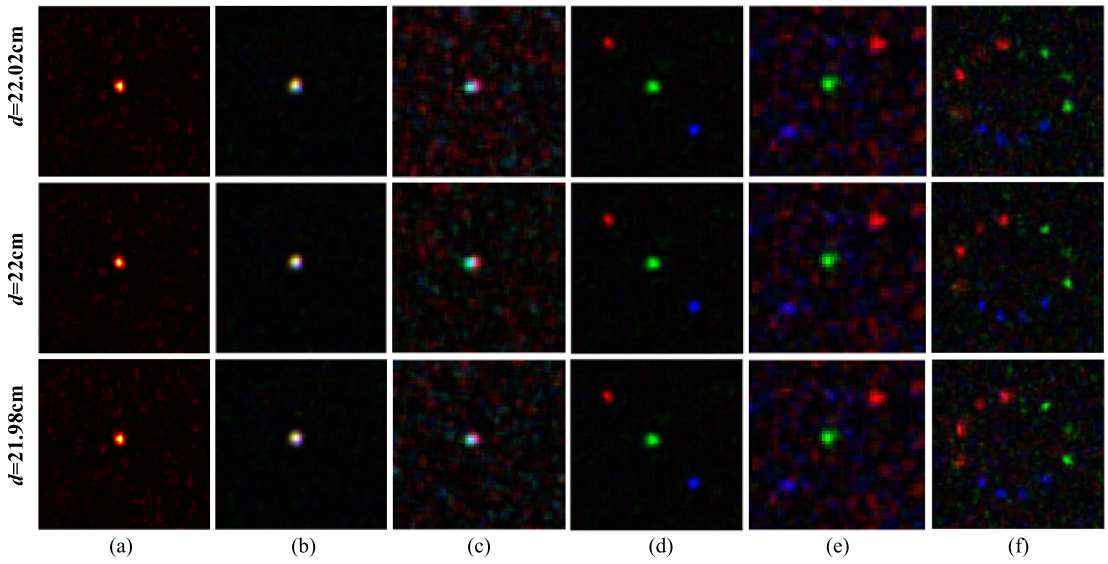

Fig. 4 Results of focusing: (a), (b) and (d) are results for monochrome focusing, single-point achromatic focusing and multi-point focusing utilizing SOTM for varied distances d = 22.02 cm, 22 cm, and 21.98 cm respectively; (c), (e) are the same as (b), (d), employing POTM; (f) is designed circular multi-point achromatic focusing.

where σ_λ is the standard deviation of the wave, x_0 is the expected value, then the relationship between FWHM and the standard deviation is

$$\text{FWHM} = 2\sqrt{2\ln 2}\sigma_\lambda. \tag{7}$$

When $\lambda = 628$ nm, 532 nm, 478 nm, the coherence length of speckles [34] are 13 pixels, 9 pixels and 8 pixels, which lead to three focusing results of 208 $\times$ 208 pixels, 144 $\times$ 144 pixels, 128 $\times$ 128 pixels for a 256 $\times$ 256 MOTM, respectively. By resize the results of 144 $\times$ 144 pixels and 128 $\times$ 128 pixels to 208 $\times$ 208 pixels, we can make the three results the same dimension (see Fig. 3(a)), with which we can focusing for different wavelengths.

After then, we scanned all the points of target on detector, which process was accomplished in a linear fashion rastering over the two-dimension pixel array as Fig. 3(b). The error is defined as the counts of deviation pixels between target point and actual point, whose pixel size is 4.2 μm $\times$ 4.2 μm. That is:

$$erf(x, y) = \sqrt{(P_{\lambda_i}(x, y) - P'_{\lambda_i}(x, y))^2} \times l \times p \tag{8}$$

where p is the pixel size of detector, l is the coherence length pixels of the speckle.

The enhancement factors [3] and error of focusing every ten segments of the detector is analyzed and shown in Fig. 3(c), (d). The enhancement factors is about 75 (see Fig. 3(c)). The pixel size of detector is 4.2 μm from Section 2 and the focusing errors of different wavelength are also in the order of sub-micron (see Fig. 3(d)). Fig. 3(e) shows the depth of focus of different wavelengths at d ranging from 0.21 cm to 0.23 cm. The depth of focus is also calculated by the FWHM of the curve in Fig. 3(e) and its computational formula is $\Delta z = 7.1\lambda(\frac{d}{D})^2$, where d is the distance between r and v, D is the area of the scatting media. When we take the variables, Δz of the averege of the three wavelengths is solved about 0.2 cm, which is also agree with the additional line in Fig. 3(e). In general, the results above show that the light can be focused with different wavelengths at arbitrary position and have the potential to be focus in 3D.

Then we further test the ability of achromatic focusing with SOTM and POTM, Fig. 4(a)–(f) display the focusing results when $N = 256$ with SOTM and POTM. The simulation results on monochrome focusing with SOTM at the central point of a 16 $\times$ 16 target in Fig. 2(a) at $d = 22.02$ cm, 22 cm and

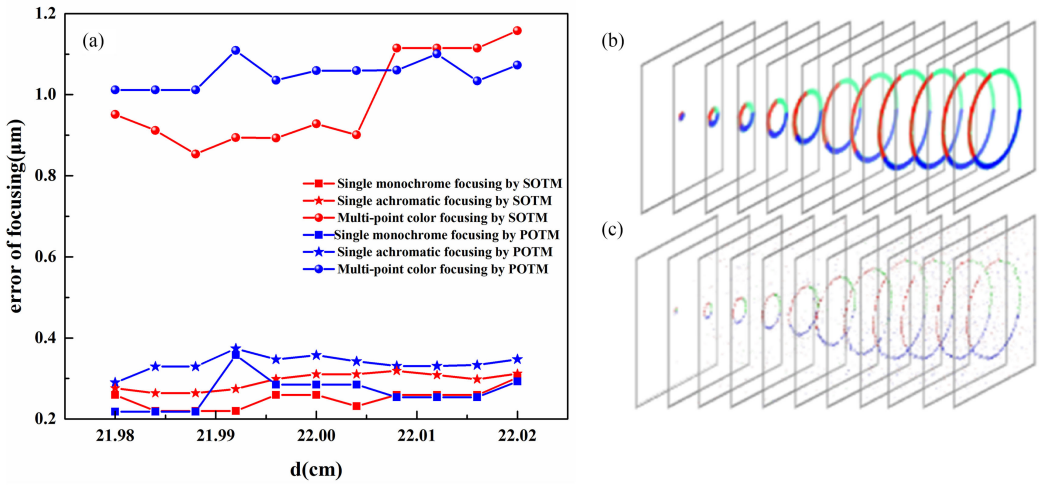

Fig. 5 Errors of focusing and achromatic 3D focusing for a circular cone:(a) the error of focusing, and blue square is the monochrome focusing with POTM without shown. The results for the focusing by SOTM and POTM are shown. (b) a 0.04 cm $\times$ 0.11 cm circular cone using 11 chipped2D slices with a step of 0.004 cm; (c) achromatic 3D result of (a).

21.98 cm are nearly the same, which reveals there exists a depth of focus to manipulate the light to get focused at different distances *d*. Interestingly, single-point achromatic focusing in the same position by SOTM in Fig. 2(b) and POTM in Fig. 4(c) also follow the law of the monochrome focusing. This result may be explained by the fact that SOTM and POTM are combined with MOTM, which can perfectly focus in different *d*. Multi-point in diagonal, negative diagonal and a polychromatic circle of light are achromatic 3D focused in Fig. 4(d)–(f), respectively.

There still exists sub-micrometer deviation of the foci position as depicted in Fig. 4(a)–(h). Here we analyze the results of Fig. 4(a)–(e) and we measure the focusing error for varied distances in Fig. 5(a). Obviously, the focusing result of monochrome wavelength has the least focusing error. On the one hand, the results show that the SOTM's focusing errors are lower than the POTM's. The inconsistency may be due to that SOTM is more accurate than POTM, which has the ability to respond to any wavelength and achromatic focusing at the expense of the various monochrome matrix dimensions and controls. On the other hand, the error of focus is increasing with the complexity of the targets, which is inevitable. However, with only a single transmission matrix, POTM brings considerable possibility for polychromatic light focusing through scattering layers.

The principle of the SOTM can be expanded to a wider range; we demonstrate that it can be used to reestablish a depth-resolved object, thanks to the existence of depth of focus, which is about 0.2 cm solved before, and the ability of focusing at arbitrary position. Here we select to display a 0.04 cm $\times$ 0.11 cm circular cone using 11 2D slices with a step of 0.004 cm (see Fig. 5(b)) and its result in Fig. 5(c) when $N = 4096$, which verifies the ability of achromatic 3D focusing with SOTM methods.

Furthermore, we also achromatic image through scattering media with SOTM. Three primary color targets and reconstruction results with dimensions of 40×40 are shown in the first and second row in Fig. 6, respectively. It can be easily seen that the second row of the Fig. 6(a)–(c) is relatively recovering the targets, and the Fig. 6(d) is the superimposed results of Fig. 6(a)–(c).Visually, the achromatic imaging result suffers a relatively low peak signal to noise ratio (PSNR) because of the dimension of the target.

To better understand the achromatic imaging through scattering by SOTM, we analyze the achromatic imaging quality of different dimensions. With different dimensions of SOTM, results for achromatic image through scattering media for 16 $\times$ 16, 20 $\times$ 20, and 30 $\times$ 30 $\sim$ 80 $\times$ 80 target are shown in Fig. 7, respectively. Intuitively, we can see that intelligibility and fidelity of the achromatic

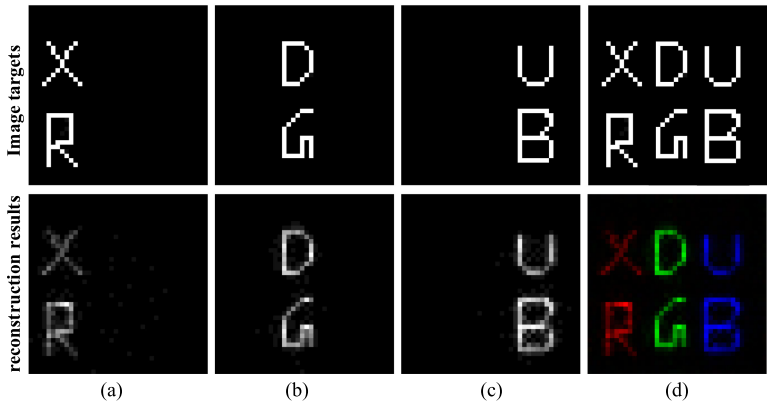

Fig. 6 Results of monochromatic imaging and achromatic imaging through scattering media with SOTM: (a) Monochromatic binary imaging targets of $\lambda = 628$ nm, 532 nm and 478 nm and achromatic imaging target. (b) Imaging results of (a).

Fig. 7 Results of serial achromatic imaging through scattering media for different dimensions. The dimensions are 16 × 16, 20 × 20, 30 × 30, 40 × 40, 50 × 50, 60 × 60, 70 × 70, 80 × 80, respectively.

imaging is proportional to the controlled SOTM dimension *N,* i.e., cells on SLM and segments on detector.

To demonstrate the applicability of the proposed methods, we also analyze the achromatic imaging quality of different dimensions numerically. The PSNR and correlation coefficient are introduced to evaluate the quality of the achromatic imaging through scattering media for different dimensions:

$$\mathrm{PSNR} = 10 log_{10}\left(\frac{\mathrm{MAX}^2}{\mathrm{MSE}}\right) \tag{9}$$

$$\mathrm{MSE} = \frac{1}{mn}\sum_{i=1}^{n}\sum_{j=1}^{m}\left\| I_{\mathrm{image}}(x,y) - I_{\mathrm{object}}(x,y)\right\|^2 \tag{10}$$

where MAX is the max of the imaging result and the MSE is the mean square error between original image I_{object} and reconstructed image I_{image}. The correlation coefficient r is calculated by:

$$r = \frac{\sum_m \sum_n \left(A_{mn} - \bar{A}\right)\left(B_{mn} - \bar{B}\right)}{\sqrt{\left(\sum_m \sum_n \left(A_{mn} - \bar{A}\right)^2\right)\sum_m \sum_n \left(B_{mn} - \bar{B}\right)^2}}, \tag{11}$$

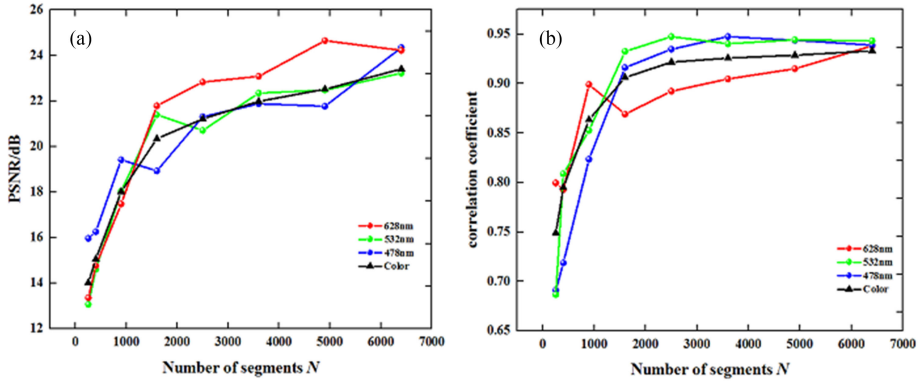

Fig. 8 PSNR and correlation coefficient of serial achromatic imaging for different dimensions of targets: (a) Curve of PSNR and matrix dimensions. (b) Curve of correlation coefficient and N.

where A denotes the intensity of the imaging target, B is the image intensities reconstructed from matrix of different dimensions.

Finally, PSNR and correlation coefficient are calculated using (9)–(11) together with the data of Fig. 7 and shown in Fig. 8(a), (b), respectively. The PSNR values increase with the demission approaching to 25 dB (see Fig. 8(a)). As the increasing of the dimensions, more monochromatic channel 'on/off' state can be controlled; therefore we can obtain higher PSNR with better quality achromatic imaging. The correlation coefficients (see Fig. 8 (b)) of the monochromatic and achromatic imaging increase with the dimensions N of the controllable channels and finally approach to 0.95. As is noted and predicted from the analysis, better quality of imaging and focusing is expected with more controllable channel N.

5. Conclusion

In summary, we demonstrate an evolutionary approach to achromatic 3D focusing and imaging through scattering media. Firstly, we present a method for focusing and imaging through scattering media based on APS. Next, we introduce the method to construct SOTM and POTM to serially and parallel 3D achromatic focus through scattering media. Besides, single point and multi-points achromatic 3D target were successfully refocused with our proposed method. The effective achromatic 3D depth of focusing in our simulation is 0.2 cm and we have done a 3D achromatic focusing for a 3D circular cone. At Last, different dimension objects displayed on the SLM were reconstructed by using the SOTM with high accuracy, which was quantified by the correlation coefficient between the reconstructed images and the target images and the PSNR of the reconstructed images. Our approach shows advantages about broadband source and the ability to programmable control the focusing and imaging. The programmable, multi-functional optical field transformation characteristics makes this system an integrated and intelligent strategy, where novel optical field transformation effect that cannot be achieve using the traditional optics can be realized by employing the WFS strategy. The results provide unexplored routes to manipulate arbitrary optical fields instead of complicated optical design and fabrication processes and the study of temporal /spectral /polarimetry speckles.

References

[1] I. M. Vellekoop, "Feedback-based wavefront shaping," *Opt. Exp.*, vol. 23, no. 9, pp. 12189–12206, May 2015.
[2] R. Horstmeyer, H. Ruan, and C. Yang, "Guide star-assisted wavefront-shaping methods for focusing light into biological tissue," *Nature Photon.*, vol. 9, no. 9, pp. 563–571, Aug. 2015.
[3] I. M. Vellekoop and A. P. Mosk, "Focusing coherent light through opaque strongly scattering media," *Opt. Lett.*, vol. 32, no. 16, pp. 2309–2311, Aug. 2007.

[4] A. Boniface *et al.*, "Transmission-matrix-based point-spread-function engineering through a complex medium," *Optica*, vol. 4, no. 1, pp. 54–59, Jan. 2017.
[5] E. G. van Putten *et al.*, "Scattering lens resolves sub-100 nm structures with visible light," *Phys. Rev. Lett.*, vol. 106, no. 19, May 2011, Art. no. 193905.
[6] X. Shao, T. Wu, and C. Gong, "Simulation on light refocusing through a highly scattering turbid medium using circular Gaussian distribution model," *Opt. Eng.*, vol. 52, no. 11, Nov. 2013, Art. no. 113104.
[7] D. B. Conkey *et al.*, "Genetic algorithm optimization for focusing through turbid media in noisy environments," *Opt. Exp.*, vol. 20, no. 5, pp. 4840–4849, Feb. 2012.
[8] D. B. Conkey, A. M. Caravaca-Aguirre, and R. Piestun, "High-speed scattering medium characterization with application to focusing light through turbid media," *Opt. Exp.*, vol. 20, no. 2, Jan. 2012, Art. no. 1733.
[9] J. Li *et al.*, "Spectrum changes produced by scattering of light with tunable spectral degree of coherence from a spatially deterministic medium," *IEEE Photon. J.*, vol. 8, no. 2, pp. 1–13, Mar. 2016.
[10] J. H. Park *et al.*, "Active spectral filtering through turbid media," *Opt. Lett.*, vol. 37. no. 15, Jul. 2012, Art. no. 3261.
[11] Z. Ansari *et al.*, "High frame-rate, 3-D photorefractive holography through turbid media with arbitrary sources, and photorefractive structured illumination." *IEEE J. Sel. Topics Quantum Electron.*, vol. 7, no. 6, pp. 878–886, Aug. 2001.
[12] C. Gong, X. Shao, and T. Wu, "Total variation optimization for imaging through turbid media with transmission matrix," *Opt. Eng.*, vol. 55, no. 12, May 2016, Art. no. 121703.
[13] Y. Ren *et al.*, "Microscopic imaging through a turbid medium by use of a differential optical Kerr gate," *IEEE Photon. Tech. Lett.*, vol. 28, no. 4, pp. 394–397, Nov. 2016.
[14] I. M. Vellekoop and M. C. Aegerter, "Scattered light fluorescence microscopy: Imaging through turbid layers," *Opt. Lett.*, vol. 35 no. 8, pp. 1245–1247, 2010.
[15] S. Popoff *et al.*, "Image transmission through an opaque material," *Nature Commun.*, vol. 1, no. 6, pp. 1–5, 2010.
[16] O. Katz *et al.*, "Focusing and compression of ultrashort pulses through scattering media," *Nature Photon.*, vol. 5 no. 6, pp. 372–377, 2011.
[17] H. He, Y. Guan, and J. Zhou. "Image restoration through thin turbid layers by correlation with a known object," *Opt. Exp.*, vol. 21 no. 10, pp. 12539–12545, 2013.
[18] S. Gigan, "Transmission matrix approach to focusing and imaging in scattering media," in *Proc. Biophoton. Congr., Biomed. Opt. Congr.*, 2018, Paper OF1D.1.
[19] O. Katz, E. Small, and Y. Silberberg. "Looking around corners and through thin turbid layers in real time with scattered incoherent light," *Nature Photon.*, vol. 6 no. 8, pp. 549–553, 2012.
[20] Z. Yin *et al.*, "Fast-forming focused spots through a multimode fiber based on an adaptive parallel coordinate algorithm," *Chin. Opt. Lett.*, vol. 13 no. 7, pp. 77–81, 2015.
[21] J. Bertolotti *et al.*, "Non-invasive imaging through opaque scattering layers," *Nature*, vol. 491, no. 7423, pp. 232–234, 2012.
[22] O. Katz *et al.*, "Non-invasive single-shot imaging through scattering layers and around corners via speckle correlations," *Nature Photon.*, vol. 8, no. 10, pp. 784–790, 2014.
[23] H. Zhuang *et al.*, "High speed color imaging through scattering media with a large field of view," *Sci. Rep.*, vol. 6, no. 1, 2016, Art. no. 32696.
[24] C. Dang, D. Tang, and S. K. Sahoo, "Single-shot multispectral imaging with a monochromatic camera," *Optica*, vol. 4, no. 10, pp. 1209–1213, 2017.
[25] J. R. Fienupet, R. G. Paxman, and T. J. Schulz, "Joint estimation of object and aberrations by using phase diversity," *J. Opt. Soc. Amer. A*, vol. 9, no. 7, pp. 1072–1085, 1992.
[26] R. G. Paxman, B. E. Stribling, B. L. Ellerbroek *et al.*, "Space object identification using phase-diverse speckle," *Proc. SPIE*, vol. 3170, pp. 2–15, 1997.
[27] S. Li *et al.*, "Imaging through scattering medias using densely connected convolutional networks," *optica*, vol. 5, no. 7, pp. 803–813, 2018.
[28] Y. Wu *et al.* "Extended depth-of-field in holographic image reconstruction using deep learning based auto-focusing and phase-recovery," *optica*, vol. 5, no. 6, pp. 704–710, 2018.
[29] S. Li *et al.*, "Dynamic imaging through turbid media based on digital holography," *J. Opt. Soc. Amer. A.*, vol. 31, no. 3, pp. 480–486, 2014.
[30] D. N. Naik *et al.*, "Real-time coherence holography," *Opt. Exp.*, vol. 18, pp. 18:13782–18:13787, 2010.
[31] M. Paturzo *et al.*, "Microscopy imaging and quantitative phase contrast mapping in turbid microfluidic channels by digital holography," *Lab. Chip*, vol. 12 no. 17, pp. 3073–3076, 2012.
[32] V. Bianco *et al.*, "Imaging through scattering microfluidic channels by digital holography for information recovery in lab on chip," *Opt. Exp.*, vol. 21 no. 20, pp. 23985–23996, 2013.
[33] E. G. Van Putten and A. P. Mosk, "The information age in optics: Measuring the transmission matrix," *Physics*, vol. 3, no. 22, 2010.
[34] S. M. Popoff *et al.*, "Controlling light through optical disordered media: Transmission matrix approach," *New J. Phys.*, vol. 13, no. 12, 2011, Art. no. 123021.
[35] A. N. Tikhonov, "Solution of incorrectly formulated problems and the regularization method," *Soviet Math. Dokl.*, vol. 5, no. 4, pp. 1035–1038, 1963.
[36] M. Born *et al.*, "Principles of optics: Electromagnetic theory of propagation, interference and diffraction of light," *Phys. Today*, vol. 53, no. 10, pp. 77–78, 2000.
[37] C. W. J. Beenakker, "Random-matrix theory of quantum transport," *Rev. Modern Phys.*, vol. 69, no. 3, pp. 731–808, 1997.
[38] J. W. Goodman, *Statistical Optics*, New York, NY, USA: Wiley, 2000.